Received: 9 September 2019 | Revised: 9 January 2021 | Accepted: 20 January 2021

DOI: 10.1002/eng2.12375

RESEARCH ARTICLE

WILEY

Fresh insights into detonation nanodiamond aggregation: An X-ray photoelectron spectroscopy, thermogravimetric analysis, and nuclear magnetic resonance study

Khabiboulakh Katsiev[1] | **Vera Solovyeva**[2] | **Remi Mahfouz**[3] | **Edy Abou-Hamad**[4] | **Wei Peng**[3] | **Hicham Idriss**[1] | **Ahmad R. Kirmani**[3]

[1]SABIC Corporate Research and Innovation Center, King Abdullah University of Science and Technology (KAUST), Thuwal, Saudi Arabia

[2]Department of Chemistry, Lomonosov Moscow State University, Moscow, Russia

[3]King Abdullah University of Science and Technology (KAUST), KAUST Solar Center (KSC), Thuwal, Saudi Arabia

[4]King Abdullah University of Science and Technology (KAUST), Thuwal, Saudi Arabia

Correspondence
Ahmad R. Kirmani, King Abdullah University of Science and Technology (KAUST), KAUST Solar Center (KSC), Thuwal 23955-6900, Saudi Arabia.
Email: ahmad.kirmani@kaust.edu.sa

Funding information
King Abdullah University of Science and Technology; Russian Science Foundation, Grant/Award Number: 18-13-00337

Abstract

Detonation nanodiamonds (DNDs) are known to be produced in aggregated clusters of a few nanometer-sized primary crystalline particles embedded in an amorphous carbon matrix exhibiting high degree of polydispersity. A commonly accepted mechanism behind DND aggregation is the bridging of primary particles via oxygen containing functionalities. Here, we provide definitive spectroscopic evidence in favor of this working mechanism by carrying out systematic chemical compositional analysis on monodispersed DND aggregates of various sizes. Oxygen content is found to increase proportionally with the aggregate size confirming the role of oxygen containing functionalities as a cross-linker. Solid-state nuclear magnetic resonance data confirms these linkers to be of ether (C—O—C) nature. Our results imply that oxygen content in DNDs can be independently tuned by varying the aggregate size, a knowledge which might benefit other applications, in addition. Next, we use this understanding to engineer the DND surfaces via an acid hydrolysis step to strip off these oxygen functionalities leading to size reduction of ca. 150 nm as-received DND aggregates to ca. 40 nm with >90% yields, without resorting to any other pre- or post-hydrolysis treatment such as surface functionalization or milling.

KEYWORDS

acid hydrolysis, aggregation, detonation nanodiamonds, ethereal bonds, nuclear magnetic resonance, thermogravimetric analysis, X-ray photoelectron spectroscopy

1 | INTRODUCTION

Detonation nanodiamonds (DNDs) are well known to aggregate.[1,2] DND aggregates (~10–500 nm) consist of primary particles ~4–5 nm in size, held together in a matrix of amorphous carbon.[1,3,4] Recent notable developments include observation of optical limitation effects in surface functionalized DNDs and the demonstration of energetic core-shell composites.[5-8] Although the potential applications of DNDs range from photonics[9] and quantum computing[10,11] to drug delivery,[12,13] they are highly size-dependent.[2] Whereas >100 nm DND aggregates would be attractive for photonics applications, the <10 nm aggregates are compatible with applications related to biosciences.[13,14] In order to be compatible

with applications, nanoparticles, in general, require high surface purity owing to their large surface-to-volume ratio, as surface-related defects adversely affect their optical and electrical properties.[2,15-19]

The aggregates contain incombustible metal and oxide impurities that should be removed before the DNDs can be employed in any application.[20] Also, Fourier transform infrared (FTIR) spectroscopy and transmission electron microscopy (TEM) results confirm that the aggregate surface is covered with undesired amorphous functionalities.[21-23] Air-oxidation at elevated temperatures has been successfully used to remove these organic surface groups, and was recently shown to enhance transverse spin-coherence time of nitrogen-vacancy centers crucial for making DNDs compatible with quantum device applications.[21,24] To completely remove the metal and oxide impurities residing inside or on the surface of the aggregates de-aggregation processes[2] such as bead milling, bead-assisted sonication, and salt-assisted dry ball milling have been used.[1,25,26]

Rate-zonal density gradient ultracentrifugation (RZDGU) has recently been employed to separate the concentrated DND colloidal suspension into various fractionation bands by weight and aggregate size – each band exhibiting significantly monodisperse aggregates of a particular size – finally obtaining highly monodispersed primary particles.[27] RZDGU presents the advantage of being a contamination-free separation approach. As the name suggests, the technique requires a density gradient media.[28,29] For DND separation, the authors employed highly concentrated aqueous solutions of sucrose as the gradient media and the DND aqueous suspension was layered on top.[27] Ultracentrifugation of the system led to a density gradient of the DNDs based on the aggregate size and weight. This gravitation-based separation approach allows separation of gram-scale amounts of DNDs in a short period rendering it a highly prospective approach for large-scale separation.

Oxygen containing functionalities on the DND surfaces and metal impurities such as iron are known to be the prime source of aggregation.[30,31] In particular, C—O—C species (ethereal) have been suggested to behave as a glue between the primary particles.[32-34] Herein, we provide direct spectroscopic evidence in support of this 'glue model'. We separate the DNDs into monodisperse bands of various aggregates sizes. This allows us to carry out systematic size-dependent chemical compositional studies using X-ray photoelectron spectroscopy (XPS) and thermogravimetric analysis (TGA), and add to a growing body of fundamental insights into size-control and aggregation.[18,35] We monitor the oxygen content and observe a correlation between the content of oxygen functionalities and the aggregate size. Oxygen content is found to scale with the aggregate size, as can be expected from the 'glue model' of aggregation. Importantly, these results demonstrate aggregate size tunability as a unique way of precisely controlling the oxygen content in DNDs. Employing nuclear magnetic resonance (NMR), these oxygen-containing species are shown to be C—O—C bonds. We, finally, target these bridges via acid hydrolysis, resulting in breaking down of the as-received DND aggregates of ca. 150 nm size to average sizes of ca. 40 nm, without resorting to any pre- or post-hydrolysis de-aggregation procedure such as milling.

2 | MATERIALS AND METHODS

2.1 | DND band preparation

The DNDs were purchased from Sigma Aldrich (Cas: 7782-40-3), and had an average size of ~150 nm with a broad size distribution as found from dynamic light scattering (DLS). DND bands were prepared using the RZDGU method, as elaborately described in literature.[27] Briefly, a customized gradient station and a six-piston fractionator (BioComp Instruments Inc) were used for preparing density gradients and band collection. A Thermo Scientific ultracentrifuge (WX Ultra 90) using a Superspin 630 rotor and Nalgene tubes (38 mL, Thermo Scientific) was utilized for centrifugation. Prior to the RZDGU process, the as-received DNDs are milled resulting in some degree of de-aggregation. The iron contaminants introduced as a result of the milling process were removed via hydrochloric acid treatment and rinsing of the milled DNDs followed by ultracentrifugation, as detailed previously.[27]

2.2 | Dynamic light scattering (DLS)

DLS (Zetasizer Nano ZS, Malvern) was used for measuring the DND aggregate sizes for the various bands, as reported elsewhere.[27] Concentration of the DND solutions was controlled by tuning the absorbance to optical density ~ 1.0 at the wavelength of 350 nm (Ocean Optics Inc., light source DH-2000-Bal, 1 cm path-length cuvette). This was done due to

sensitivity of the measurement to solution concentration as reported previously,[27] and was achieved by dilution with an aqueous HCl solution (pH ~ 3.8) before each DLS measurement.

2.3 | Transmission electron microscopy (TEM)

TEM images were obtained using a TitanG^2 80-300 instrument, equipped with an image-corrector from CEOS. Two microliters of DNDs suspended in water was deposited on ultrathin carbon-coated films on 300 mesh copper grids and dried in air for at least 1 h. DNDs were subjected to re-aggregation during the drying process in preparation of TEM grids. Shenderova et al suggested that re-aggregation can be largely circumvented by dispersing DNDs in dimethyl sulfoxide (DMSO)/Methanol mixture.[36] Here, we dispersed the dried sample powder in DMSO followed by the addition of an equal volume of methanol to the solution. The mixture was then sonicated (sonication bath: Bransonic, Mexico) for 1 h, followed by deposition onto the ultrathin TEM grids.

2.4 | X-ray photoelectron spectroscopy (XPS)

The DND samples were prepared by drop-casting an aqueous solution onto a high purity (99.9%) copper (Cu) foil, and air-dried. To ensure complete drying of the DNDs, the samples were left in the ultra-high vacuum (UHV) load-lock chamber under vacuum for ~20 min before beginning the XPS measurements. Measurements were carried out in anUHV chamber with a base pressure of $<1 \times 10^{-9}$ mbar. The chamber was equipped with a SPHERA U7 hemispherical energy analyzer with 7 channel detector. Monochromated X-rays were generated using XM 1000, a high intensity, high energy resolution monochromated Al K_α X-ray source with 500 mm Rowland circle diameter, minimum spot size ~1 mm, photon line width < 250 meV. Spectra were acquired at normal emission using Al K_α (1486.6 eV). The photoelectrons were collected by the hemispherical energy analyzer operated in constant analyzer energy (CAE) mode. A charge neutralizing electron flood gun was used to circumvent the effects of sample charging. The electron flux of the neutralizing gun was optimized such as the sp^2 carbon peak in the samples was fixed at 284.8 eV. Each sample was analyzed 1–3 times. The analyzed area was ~1 mm^2. A pass energy of 40 eV was used for the survey spectrum, which was averaged over three scans. The higher resolution core-level spectra utilized a pass energy of 10 eV and multiple scans depending on the signal intensity (~10 scans for C1s peaks, ~80 scans for N1s peaks). CasaXPS was used for analysis and fitting of the peaks. A mix of Gaussian and Lorentzian line-shapes, GL(30), was used for peak-fitting, and a Shirley background removal was performed. Relative atomic concentrations were calculated using the high-resolution core-level peaks for higher accuracy, considering appropriate relative sensitivity factors.

2.5 | Solid-state NMR

1D ^{13}C CP/MAS and MAS spectra were recorded on a Bruker AVANCE III spectrometer operating at ^{1}H resonance frequency of 600 MHz, and using a conventional double resonance 3.2 mm CPMAS probe. The samples were introduced under argon into zirconia rotors, which were then tightly closed. The spinning frequency was set to 10 kHz for the ^{13}C analyses. NMR chemical shifts are reported with respect to tetramethylsilane as the external reference. For CP/MAS ^{13}C NMR experiments, the following sequence was used: (i) 90° pulse on the proton (pulse length 2.4 μs), then cross-polarization step with a contact time of 2 ms. The delay scans were set to 5 s to allow complete relaxation of the ^{1}H nuclei, and 20,000 scans were performed for a carbon experiment. An apodization function (exponential) corresponding to a line broadening of 80 Hz was applied prior to Fourier transformation. For the ^{13}C MAS NMR experiment under high-power proton decoupling (hpdec), the delay scans were set to 30 s to allow the complete relaxation and 10,000 scans were performed. For these measurements, the as-received DNDs were oxidized following a protocol reported earlier by Osswald et al.[21] Briefly, this involves oxidizing the aggregates at 425°C for 5 h.

2.6 | Thermo-gravimetric analysis

TGA analysis was carried out in alumina crucibles under argon flow (Netzsch, TG 209 F1 with ASC). A heating rate of 5°C/min and sample mass of ca. 12 mg were set for the measurements.

2.7 | Attenuated total reflectance Fourier transform infrared spectroscopy (ATR-FTIR)

ATR-FTIR data were collected on a Thermo Scientific Nicolet iS50 instrument equipped with nitrogen purge and aligned for signal clarity. The instrument was calibrated before sampling against a newly cleaned (acetone) and dried crystal surface. Solid DND samples were placed directly on the crystal and secured with the needle press. Scans (64) from 4000 to 900 cm^{-1} were recorded.

2.8 | Acid hydrolysis

Acid hydrolysis of the DNDs was performed following published procedure.[37] DNDs (100 mg) were refluxed in 3 M nitric acid (10 mL) for 24 h. Reaction mixture was cooled to room temperature, centrifuged, supernatant was discarded, and the solid precipitate was rinsed with DI water and centrifuged three times till neutral. The solid residue was dispersed in 4 M NaOH (5 mL), centrifuged and rinsed with DI water till neutral, followed by drying in air.

3 | RESULTS AND DISCUSSION

In this study, we deployed the RZDGU method for separating the DND aggregates into bands of different aggregate sizes. The details of the method have been comprehensively outlined elsewhere.[27] We separated the concentrated DND colloidal suspension into six bands of highly monodispersed DNDs with the following sizes: (12.5 ± 7.6) nm, (20.9 ± 12.8) nm, (30.6 ± 11.7) nm, (35.5 ± 12.6) nm, (44 ± 15.1) nm, and (47.2 ± 16.4) nm for the bands 1 through 6 respectively (as estimated from DLS measurements reported earlier[27]). Each band of monodispersed DNDs can therefore be studied separately. Taking into account the size of an individual primary particle of *ca* ~ 5 nm, it is suggested that the increase of the size of aggregates from band 1 through 6 occurs by adding a few tens of primary particles per band.

The morphology of the DND bands was studied by TEM and showed that they consist of aggregates of several crystalline primary particles as demonstrated in Figure 1 where the first, third, and the sixth bands are shown. The DND aggregate size is found to increase from (A) to (C). The images distinctly show the primary crystalline particles clustering together to form aggregates.

The DNDs demonstrated chemical purity as found by XPS. Figure S1 shows the survey spectrum for band 6: with C as the main component (~91% relative atomic concentration), followed by O (~8%), N (~1%), and negligible traces of Cl. Chlorine is an impurity and is present due to the hydrochloric acid treatment (as part of sample preparation procedure).

Oxygen content, determined from XPS, is found to depend on the aggregate size as evident from O1s core level peak analysis (oxygen atomic concentration normalized to the carbon concentration), shown in Figure 2(A) (please refer to Table S1). The oxygen content has been primarily ascribed to the oxygen bonded to carbon (please see Figure S2 and the following discussion).[5]

The monotonic increase of oxygen with the DND aggregate size can be explained if we assume the DND aggregates to be spherical (for simplicity of geometric considerations). Figure 2(B) shows the net volume of the DND aggregates in the

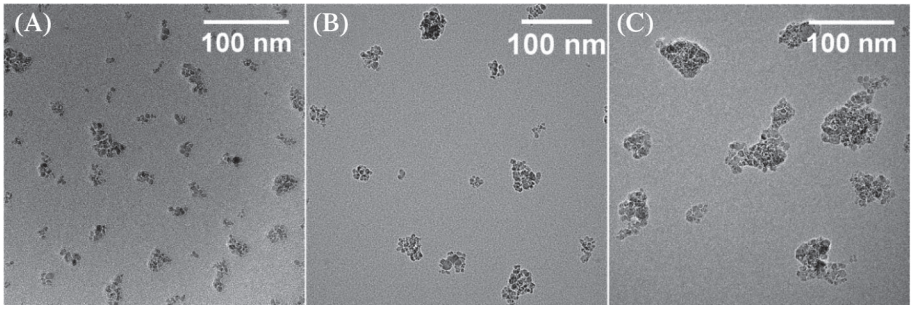

FIGURE 1 TEM images of DND aggregates consisting of several crystalline primary particles. (A) DND aggregates obtained in the Band 1. Small aggregates consisting of a few primary particles are observed. (B) The aggregate size increases for the Band 3 owing to increased aggregation. Particle size reaches a maximum for the Band 6 as shown in (C). Aggregate size was found to increase as: 12.5 nm (Band 1), 30.6 nm (Band 3), and 47.2 nm (Band 6)

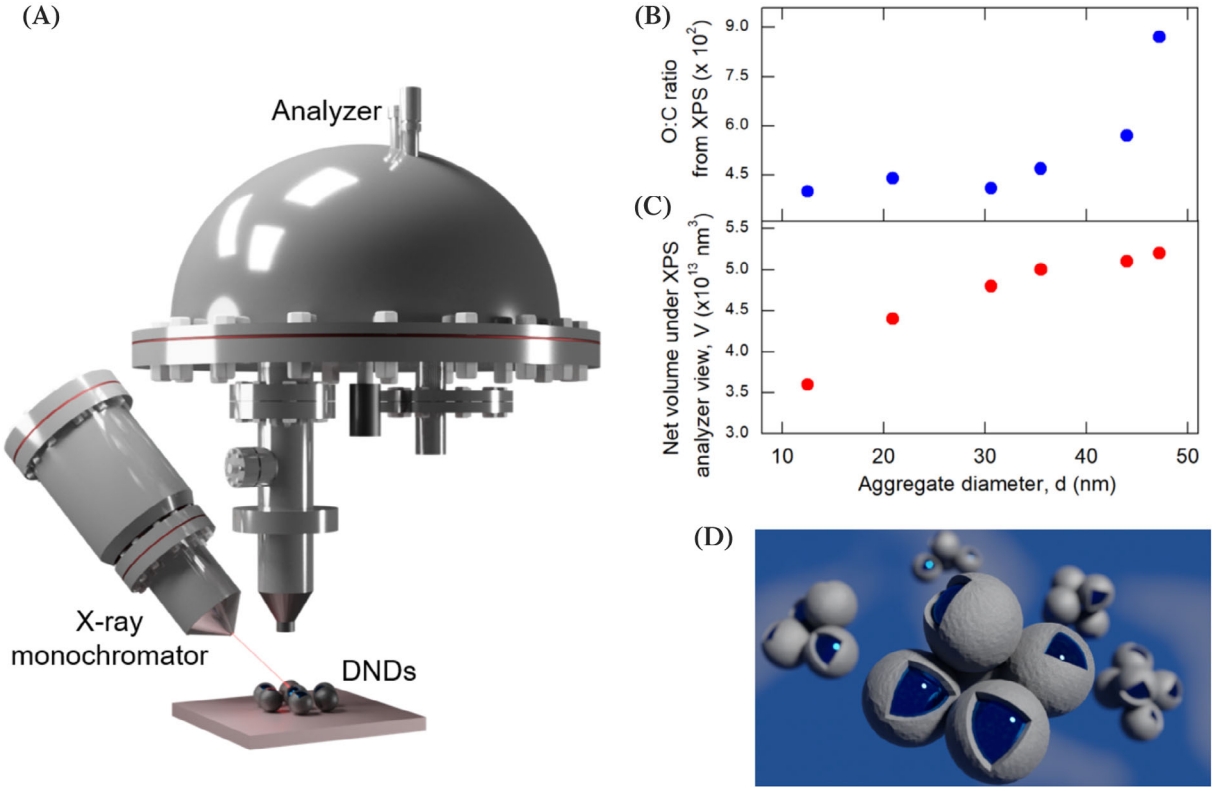

FIGURE 2 (A) Experimental setup for the XPS measurements. (B) Oxygen-to-carbon ratio for the various DND bands obtained from XPS C1s is plotted as a function of the DND aggregate size. Oxygen content is found to increase monotonically with aggregate size. (C) Net DND aggregate volume under the XPS analyzer field of view (V) is plotted as a function of the aggregate size. V is found to have a monotonic dependence on the size, similar to (A). (D) Schematic showing aggregated DNDs. Primary crystalline cores (shiny blue surfaces) are tethered together by ethereal bonds residing in the sp^2-shells (gray) leading to aggregate formation

field of the view of the XPS analyzer (V), as a function of the aggregate size. V is also found to increase monotonically with the aggregate size. Calculation of V is crucial in interpreting the XPS data, since the measured oxygen content is directly associated with this volume. Mathematical derivation of V has been shown in the SI (also see Table S2). The increase in Figure 2(B) makes it obvious that the oxygen content of DND aggregates increases proportionally with their volume (i.e., the net volume under the XPS analyzer field of view). Although the exact dependence of oxygen on the aggregate size is difficult to extract from this data and further finely spaced bands might be needed, the increase in oxygen content for bands 5 and 6 is obvious. On the other hand, the increase in volume appears to be less prominent for these bands. It is possible that larger DNDs aggregates, such as in bands 5 and 6, have significantly higher amounts of oxygen, compared to smaller aggregates (non-linear dependence). Therefore, even though the volume being probed by the XPS analyzer increases less prominently, the oxygen content per unit probed-volume rises sharply for larger aggregates.

The sp^2 content in the aggregates, determined by TGA and known to carry the oxygen functionalities,[21] is also expectedly found to increase with aggregate size, as shown in Figure S3.

This correlation between the oxygen functionalities (XPS) and sp^2 content (TGA) on the aggregate size supports the 'glue model' of DND aggregation wherein oxygen resides in the sp^2 shells and behaves as a 'glue' holding primary particles together leading to aggregation (Figure 2(C)).[32-34] Equally important, the above-discussed correlation also suggests that the oxygen content in DNDs can be independently tuned by varying the aggregate size. We believe this unique handle on surface functionalization can have benefits for specific applications.

The above-observed dependence seems to suggest that the packing density of the irregularly shaped primary particles (forming the aggregates) decreases with aggregate size.[38,39] In other words, increasing aggregate size might be leading to an increased porosity, thereby, requiring more oxygen content. This might be linked to the packing behavior of the primary particles. In general, nanoparticles are known to assemble in ordered or disordered geometries depending upon the interplay among the various participating forces: Van der Waals, chemical or electrostatic.[40-42] It has been reported

that strong electrostatic repulsions can lead to a reduced nanoparticle packing density for the ensemble.[43] However, a detailed investigation of the packing of primary particles in the current case and its impact on the overall packing density for the various aggregates is out of the scope of this study.

In fact, oxidation is known to enhance the mechanical properties including interfacial bonding in various carbon nanomaterials, such as, carbon fiber.[44-46] Oxygen atoms introduced via ultraviolet/ozone treatment have been suggested to enhance adhesion of carbon fibers to resin matrices by introducing surface functionalities such as alkoxide, carbonyl and carboxyl groups.[47,48] Using XPS analysis, enhancement of alcohol adsorption on the surface of non-porous carbon fibers was demonstrated by increasing the surface oxygen.[48] However, determination of the exact chemical nature of oxygen functionalities with XPS has an intrinsic ambiguity owing to the overlap of high binding energy (BE) components (please see Figures S4 and S5, Table S3 and the associated discussion). Various species such as ethers, alkoxy group, cyano group and halogenated carbon can all be expected in the rather narrow BE window of ~1 eV (286–287.5 eV).[15]

Therefore, in order to reveal the nature of oxygen functionalities responsible for the aggregation of DNDs, we carried out solid-state nuclear magnetic resonance (SS-NMR) spectroscopy. NMR is a powerful tool to study the structural features and determination of different allotropic forms in nanocarbons since the position of the NMR signal of each nucleus depends on the nature of chemical bonding.

As hydrogenated carbons could exist in DNDs, ^{1}H-^{13}C cross-polarization magic angle spinning (CP/MAS) NMR spectrum with a spinning rate of 10 kHz was recorded favoring carbon atoms in the neighborhood of ^{1}H nuclei, as shown in Figure 3(A). The technique allows the detection of carbon atoms from the surface and one or two near-surface layers. CP/MAS reveals a line at 45 ppm which is typical of aliphatic carbons and is assigned to CH and CH_2 groups in accordance with literature reports[22,49-54] (the sample contains COH groups, which exhibit a ^{13}C chemical shift of 75 ppm). The CH, CH_2, and COH peaks are found to be smaller as compared to the reports by Dubois and Panich,[49-54] indicating that oxidation results in a drastic reduction in the number of hydrocarbon groups. Interestingly, the CP/MAS reveals two peaks at 35 and 37 ppm, whereas only one peak was observed at 35 ppm by Dubois and Panich which was assigned to sp^3 hybridized carbons corresponding to the diamond phase.[49-54] The first peak at 35 ppm can be attributed to a highly ordered crystalline diamond phase, which usually shows a sharp line width. The second, broader component observed at 37 ppm can be attributed either to a distorted sp^3 system due to environmental perturbation such as crystal lattice defects, to a disordered crystalline phase, or to distorted tetrahedral coordination.[52] The ^{13}C NMR spectra of the DNDs were also recorded with MAS (Figure 3(B)) with a spinning rate of 10 kHz. In this experiment, ^{1}H decoupling was applied. A broad resonance line at 33 ppm is observed which is assigned to sp^3 hybridized carbons in the diamond core. Besides this, a weak signal

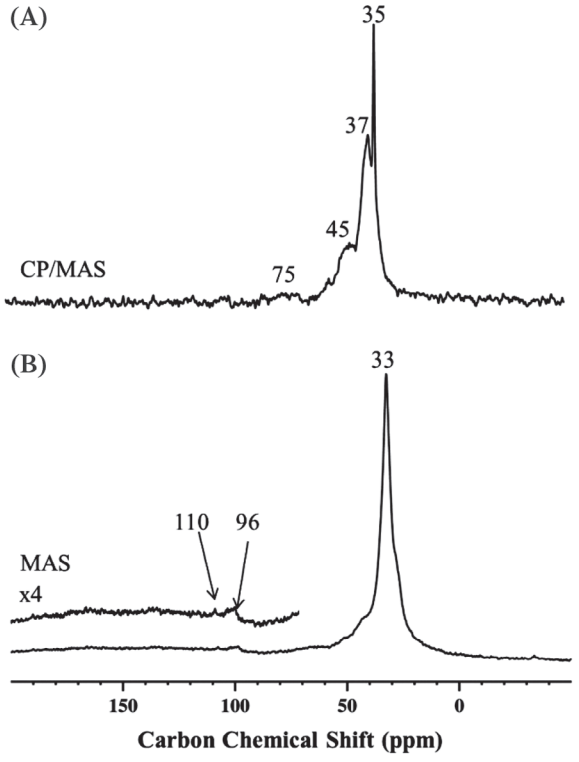

FIGURE 3 (A) CP/MAS and (B) MAS ^{13}C NMR spectra for the as-received DNDs after oxidation

was detected at 110 ppm which can be assigned to aromatic sp^2 carbons (C=C) of the graphitic shell. It should be noted that the detection of these signals, which are small not only in absolute terms but also relative to the two-orders of magnitude larger peak at 33 ppm, requires careful measurement.[55] No signal was detected between 170 and 180 ppm in MAS and CP/MAS that can be assigned to carbonyls (C=O).[49-54] Most importantly, the ^{13}C MAS NMR spectrum shows an additional high frequency peak at 96 ppm that was assigned to carbon atoms in the disordered DND shell and corresponds to the C—O—C chemical shift position. This allows identification of the exact chemical nature of the oxygen functionalities responsible for the observed aggregation, suggesting that ethereal functionalities act as a cross-linker between primary crystalline particles. This confirmation agrees with the view that C—O—C species are responsible for bridging of DND primary particles leading to aggregation. Indeed, previous reports have shown a significant reduction of C—O—C species upon de-aggregation using FTIR.[32-34] The C—O—C peak in ^{13}C MAS NMR is small because the relaxation delay is very long compared to the others peaks. In addition, there are no protons or free electrons around this linker. For this reason, there is no peak in the cross-polarization spectra and only a small peak on the direct-polarization MAS. Although NMR is a highly sensitive technique, occasionally it cannot be quantitative because of different relaxation delays.

Finally, as a proof-of-concept, we employed nitric acid hydrolysis to target these oxygen-containing functionalities in the as-received DNDs and demonstrated size reduction. The initially ca. 150 nm aggregates were found to successfully break down to ca. 40 nm without resorting to any other physical or chemical de-aggregation technique, such as surface treatment or milling. Figure 4 shows the particle size distributions obtained from DLS for the as-received and acid-hydrolyzed DNDs. As shown in Table S4, ca. 98% of the as-received aggregates were successfully de-aggregated with yields >90%.

As is known, FTIR is an important tool to analyze the surface chemistry of DNDs, besides XPS.[35,56-58] We carried out FTIR measurements on the as-received and acid-hydrolyzed DNDs to confirm removal of C—O—C species. Results are shown in Figure S6. The sharp band at ~3690 cm^{-1} belongs to —OH stretch of free water, broad band at ~3380 cm^{-1} belongs to —OH stretch vibrations of alcohol functions, overlaid band with maxima at 3320 cm^{-1} belong to water —OH bending vibrations and the doubled band with a shoulder at 2930–2850 cm^{-1} is representing CH_x stretching vibrations.[56] The appearance of these signals is common for both types of DNDs (i.e., as-received and acid-hydrolyzed).

FTIR spectrum of the as-received DND possesses strong intensity absorption at ~1720 cm^{-1} that belongs to the carbonyl signal of the carboxylic acid or/and keto-groups. Signals at 1635 cm^{-1} are ascribed to stretching vibration of C—O group in carboxylic function. Absorbance at ~1600 cm^{-1} belongs to C=C stretching vibrations of carbon–carbon double bond. Broad absorbance signals in the range 1400–1000 cm^{-1} represent various vibrations of C—O and C—O—C bonds and overlap with bending vibrations of C=C function. Among these signals, the bands at ~1390 cm^{-1} and 1330 cm^{-1} belong to CH_x bending vibrations of C=C, band at 1250 cm^{-1} belongs to C—O—C ether-like bending, while 1100 cm^{-1} is the C—O bending band.

After the treatment of DNDs with nitric acid, the signal at ~1720 cm^{-1} showed noticeable decrease of intensity that corresponds to decrease of carbonyl groups. A strong intensity band appeared at 1636 cm^{-1} that corresponds to O—H of adsorbed water. Relative intensity of bands at 1250 cm^{-1} and 1130 cm^{-1} drastically decreased confirming reduction of the C—O—C ether species.

Overall, our experimental data supports the 'glue model' proposed by Xu and Xue, where C—O—C bridges between DNDs were suggested to result in aggregation.[33] sp^2 carbon has been earlier shown to cause aggregation in DNDs,[21]

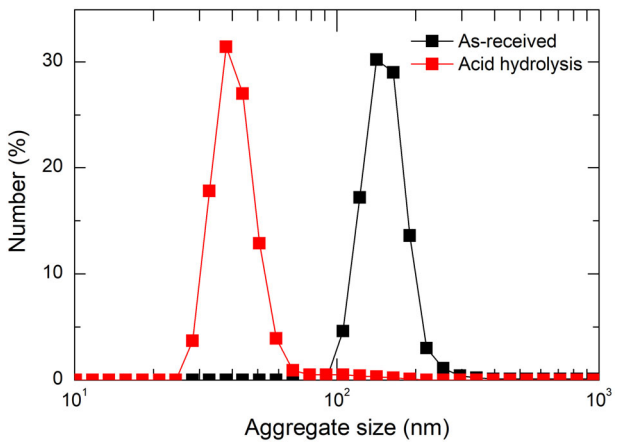

FIGURE 4 DLS data showing particle size distributions of the DND aggregates (by number). Acid hydrolysis (red) leads to size reduction

however, identifying the exact functional group responsible for aggregation has remained challenging. This is understandable given the complex nature of the sp^2-shell, believed to consist of graphite, nano-onions, amorphous carbon and various sp^2-carbon containing functional groups. We have provided evidence from NMR and FTIR that unambiguously identifies C—O—C as the group responsible for aggregation. Likely, the C—O—C species resides in the sp^2 shells. An increase in sp^2 content with aggregate size, as observed in TGA, therefore points toward an increasing C—O—C content.

4 | CONCLUSIONS

We have carried out a detailed chemical compositional analysis of monodispersed DND aggregates of various sizes obtained via RZDGU. Employing XPS, TGA, and SS-NMR, we find that oxygen content increases with the aggregate size, substantiating the oxygen-led-aggregation model. These observations open the possibility of independently tuning the oxygen content in DNDs via precise aggregate size control. Finally, we employ nitric acid hydrolysis to break down the C—O—C bridges leading to successful de-aggregation of the as-received aggregated DNDs. Acid hydrolysis reduces 98% of the ca. 150 nm aggregates down to ca. 40 nm with >90% yields, without resorting to any pre- or post-hydrolysis de-aggregation technique. There is room for optimization of the hydrolysis process targeting further size reductions and possibly single-digit sizes, and should be focus of future research in this direction. Our study opens routes to de-aggregating DNDs in a low-cost and facile manner for a variety of applications, including, quantum computing and biology.

ACKNOWLEDGMENTS

The research reported in this publication was supported by funding from King Abdullah University of Science and Technology (KAUST). K.K., R. M., and A.R.K. would like to thank Prof. Osman M. Bakr of KAUST Catalysis Center (KCC), KAUST for his continuous support and encouragement. The work of V.S. was supported by the Russian Science Foundation grant 18-13-00337.

PEER REVIEW INFORMATION

Engineering Reports thanks the anonymous reviewers for their contribution to the peer review of this work.

DATA AVAILABILITY STATEMENT

The data that support the findings of this study are available from the corresponding author upon reasonable request.

CONFLICT OF INTEREST

The authors declare no potential conflict of interest.

AUTHOR CONTRIBUTIONS

Khabiboulakh Katsiev: Conceptualization; methodology; writing-review and editing. **Vera Solovyeva:** Investigation. **Remi Mahfouz:** Methodology. **Edy Abouhamad:** Investigation. **Wei Peng:** Methodology. **Hicham Idriss:** Writing-review and editing. **Ahmad Kirmani:** Conceptualization; methodology; project administration; supervision; writing-original draft; writing-review and editing.

ORCID

Ahmad R. Kirmani https://orcid.org/0000-0002-8351-3762

REFERENCES

1. Krüger A, Kataoka F, Ozawa M, et al. Unusually tight aggregation in detonation nanodiamond: identification and disintegration. *Carbon*. 2005;43(8):1722-1730.
2. Mochalin VN, Shenderova O, Ho D, Gogotsi Y. The properties and applications of nanodiamonds. *Nat Nanotechnol*. 2012;7(1):11-23.
3. Ōsawa E. Recent progress and perspectives in single-digit nanodiamond. *Diamond Relat Mater*. 2007;16(12):2018-2022.
4. Shenderova OA, Barnard AS, Gruen DM. *1 - Carbon family at the Nanoscale. Ultrananocrystalline Diamond*. Vol 3-22. Norwich, NY: William Andrew Publishing; 2006.
5. Guillevic M, Pichot V, Fioux P, Schnell F, Spitzer D. Nanodiamond-based energetic core-shell composites: the route towards safer materials. *Diamond Relat Mater*. 2019;93:150-158.

6. Pichot V, Guerchoux M, Muller O, et al. Nanodiamond coating by polyethylenimine for optical limitation. *Diamond Relat Mater*. 2019;95:55-59.
7. Muller O, Pichot V, Merlat L, Spitzer D. Optical limiting properties of surface functionalized nanodiamonds probed by the Z-scan method. *Sci Rep*. 2019;9(1):519.
8. Pichot V, Muller O, Seve A, Yvon A, Merlat L, Spitzer D. Optical properties of functionalized nanodiamonds. *Sci Rep*. 2017;7(1):14086.
9. Grichko V, Tyler T, Grishko VI, Shenderova O. Nanodiamond particles forming photonic structures. *Nanotechnology*. 2008;19(22):225201.
10. Neumann P, Beck J, Steiner M, et al. Single-shot readout of a single nuclear spin. *Science*. 2010;329(5991):542-544.
11. Holt KB. Diamond at the nanoscale: applications of diamond nanoparticles from cellular biomarkers to quantum computing. *Philos Trans R Soc London A Math Phys Eng Sci*. 2007;365(1861):2845-2861.
12. Chow EK et al. Nanodiamond therapeutic delivery agents mediate enhanced chemoresistant tumor treatment. *Sci Transl Med*. 2011;3(73):73ra21-73ra21.
13. Mochalin VN, Gogotsi Y. Biomedical Applications of Diamond Nanoparticles. *ECS Meeting Abstracts*. Chicago, IL; 2015. http://dx.doi.org/10.1149/ma2015-01/5/766.
14. Schrand AM, Hens SAC, Shenderova OA. Nanodiamond particles: properties and perspectives for bioapplications. *Crit Rev Solid State Mater Sci*. 2009;34(1–2):18-74.
15. Kirmani AR, Peng W, Mahfouz R, et al. On the relation between chemical composition and optical properties of detonation nanodiamonds. *Carbon*. 2015;94:79-84.
16. Kirmani AR, Carey GH, Abdelsamie M, et al. Effect of solvent environment on colloidal-quantum-dot solar-cell manufacturability and performance. *Adv Mater*. 2014;26(27):4717-4723.
17. Katsiev K, Ip AH, Fischer A, et al. The complete in-gap electronic structure of colloidal quantum dot solids and its correlation with electronic transport and photovoltaic performance. *Adv Mater*. 2014;26(6):937-942.
18. Stehlik S, Varga M, Ledinsky M, et al. Size and purity control of HPHT Nanodiamonds down to 1 nm. *J Phys Chem C*. 2015;119(49):27708-27720.
19. Krueger A, Lang D. Functionality is key: recent progress in the surface modification of Nanodiamond. *Adv Funct Mater*. 2012;22(5):890-906.
20. Dolmatov YV. Detonation synthesis ultradispersed diamonds: properties and applications. *Russ Chem Rev*. 2001;70(7):607-626.
21. Osswald S, Yushin G, Mochalin V, Kucheyev SO, Gogotsi Y. Control of sp2/sp3 carbon ratio and surface chemistry of nanodiamond powders by selective oxidation in air. *J Am Chem Soc*. 2006;128(35):11635-11642.
22. El Tall O et al. Direct functionalization of nanodiamonds with maleimide. *Chem Mater*. 2014;26(9):2766-2769.
23. Costa GCC, Shenderova O, Mochalin V, Gogotsi Y, Navrotsky A. Thermochemistry of nanodiamond terminated by oxygen containing functional groups. *Carbon*. 2014;80:544-550.
24. Tsukahara R, Fujiwara M, Sera Y, et al. Removing non-size-dependent electron spin decoherence of nanodiamond quantum sensors by aerobic oxidation. *ACS Appl Nano Mater*. 2019;2(6):3701-3710.
25. Ozawa M, Inaguma M, Takahashi M, Kataoka F, Krüger A, Ōsawa E. Preparation and behavior of brownish. *Clear Nanodiamond Colloids Adv Mater*. 2007;19(9):1201-1206.
26. Pentecost A, Gour S, Mochalin V, Knoke I, Gogotsi Y. Deaggregation of nanodiamond powders using salt- and sugar-assisted milling. *ACS Appl Mater Interfaces*. 2010;2(11):3289-3294.
27. Peng W, Mahfouz R, Pan J, Hou Y, Beaujuge PM, Bakr OM. Gram-scale fractionation of nanodiamonds by density gradient ultracentrifugation. *Nanoscale*. 2013;5(11):5017-5026.
28. Komatsu N, Wang F. A comprehensive review on separation methods and techniques for single-walled carbon nanotubes. *Materials*. 2010;3(7):3818-3844.
29. Graham JM. *Biological Centrifugation*. London: Bios; 2001.
30. Kulakova II. Surface chemistry of nanodiamonds. *Phys Solid State*. 2004;46(4):636-643.
31. Aleksenskiy AE, Eydelman ED, Vul AY. Deagglomeration of detonation nanodiamonds. *Nanosci Nanotechnol Lett*. 2011;3(1):68-74.
32. Williams OA, Hees J, Dieker C, Jäger W, Kirste L, Nebel CE. Size-dependent reactivity of diamond nanoparticles. *ACS Nano*. 2010;4(8):4824-4830.
33. Xu K, Xue Q. Deaggregation of ultradispersed diamond from explosive detonation by a graphitization–oxidation method and by hydroiodic acid treatment. *Diamond Relat Mater*. 2007;16(2):277-282.
34. Xu X, Yu Z. Influence of thermal oxidation on as-synthesized detonation nanodiamond. *Particuology*. 2012;10(3):339-344.
35. Jirásek V et al. Plasma treatment of detonation and HPHT nanodiamonds in diffuse coplanar surface barrier discharge in H2/N2 flow. *Phys Status Solidi (a)*. 2016;213(10):2680-2686.
36. Shenderova O, Hens S, McGuire G. Seeding slurries based on detonation nanodiamond in DMSO. *Diamond Relat Mater*. 2010;19(2–3):260-267.
37. Shao L et al. Removal of amorphous carbon for the efficient sidewall functionalisation of single-walled carbon nanotubes. *Chem Commun*. 2007;47:5090-5092.
38. Zangmeister CD, Radney JG, Dockery LT, et al. Packing density of rigid aggregates is independent of scale. *Proc Natl Acad Sci*. 2014;111(25):9037-9041.
39. Pefferkorn E. Chapter 17 The cohesion of fractal agglomerates: an elementary numerical model. In: Agba MG, Salman D, Michael JH, eds. *Handbook of Powder Technology*. Elsevier Science B.V.; 2007:741-791.

40. Shevchenko EV, Talapin DV. *Self-assembly of semiconductor nanocrystals into ordered superstructures*. In: Rogach AL, ed. *Semiconductor Nanocrystal Quantum Dots: Synthesis, Assembly, Spectroscopy and Applications*. Vienna, Austria: Springer; 2008:119-169.
41. Min Y, Akbulut M, Kristiansen K, Golan Y, Israelachvili J. The role of interparticle and external forces in nanoparticle assembly. *Nat Mater*. 2008;7(7):527-538.
42. Hanrath T, Choi JJ, Smilgies D-M. Structure/processing relationships of highly ordered Lead salt Nanocrystal Superlattices. *ACS Nano*. 2009;3(10):2975-2988.
43. Xia Y, Nguyen TD, Yang M, et al. Self-assembly of self-limiting monodisperse supraparticles from polydisperse nanoparticles. *Nat Nanotechnol*. 2011;6(9):580-587.
44. Qian X, Zhi J, Chen L, Huang J, Zhang Y. Effect of low current density electrochemical oxidation on the properties of carbon fiber-reinforced epoxy resin composites. *Surf Interface Anal*. 2013;45(5):937-942.
45. Kettle AP, Beck AJ, O'Toole L, Jones FR, Short RD. Plasma polymerisation for molecular engineering of carbon-fibre surfaces for optimised composites. *Compos Sci Technol*. 1997;57(8):1023-1032.
46. Jones C. Special issue interfaces in composites the chemistry of carbon fibre surfaces and its effect on interfacial phenomena in fibre/epoxy composites. *Compos Sci Technol*. 1991;42(1):275-298.
47. Osbeck S, Bradley RH, Liu C, Idriss H, Ward S. Effect of an ultraviolet/ozone treatment on the surface texture and functional groups on polyacrylonitrile carbon fibres. *Carbon*. 2011;49(13):4322-4330.
48. Osbeck S, Ward S, Idriss H. Effect of UV and electrochemical surface treatments on the adsorption and reaction of linear alcohols on non-porous carbon fibre. *Appl Surf Sci*. 2013;270:272-280.
49. Dubois M, Guérin K, Batisse N, et al. Solid state NMR study of nanodiamond surface chemistry. *Solid State Nucl Magn Reson*. 2011;40(4):144-154.
50. Dubois M, Guérin K, Petit E, et al. Solid-state NMR study of nanodiamonds produced by the detonation technique. *J Phys Chem C*. 2009;113(24):10371-10378.
51. Panich AM. Solid state nuclear magnetic resonance studies of nanocarbons. *Diamond Relat Mater*. 2007;16(12):2044-2049.
52. Panich AM. Nuclear magnetic resonance studies of Nanodiamonds. *Crit Rev Solid State Mater Sci*. 2012;37(4):276-303.
53. Panich AM, Aleksenskii AE. Deaggregation of diamond nanoparticles studied by NMR. *Diamond Relat Mater*. 2012;27–28:45-48.
54. Panich AM et al. Nuclear magnetic resonance study of ultrananocrystalline diamonds. *Eur Phys J B*. 2006;52(3):397-402.
55. Cui JF, Fang XW, Schmidt-Rohr K. Quantification of C=C and C=O surface carbons in detonation Nanodiamond by NMR. *J Phys Chem C*. 2014;118(18):9621-9627.
56. Stenclova P, Celedova V, Artemenko A, et al. Surface chemistry of water-dispersed detonation nanodiamonds modified by atmospheric DC plasma afterglow. *RSC Adv*. 2017;7(62):38973-38980.
57. Kromka A et al. Low-temperature hydrogenation of diamond nanoparticles using diffuse coplanar surface barrier discharge at atmospheric pressure. *Physica Status Solidi (b)*. 2015;252(11):2602-2607.
58. Kozak H, Artemenko A, Čermák J, Švrček V, Kromka A, Rezek B. Oxidation and reduction of nanodiamond particles in colloidal solutions by laser irradiation or radio-frequency plasma treatment. *Vibr Spectrosc*. 2016;83:108-114.

SUPPORTING INFORMATION

Additional supporting information may be found online in the Supporting Information section at the end of this article.

How to cite this article: Katsiev K, Solovyeva V, Mahfouz R, et al. Fresh insights into detonation nanodiamond aggregation: An X-ray photoelectron spectroscopy, thermogravimetric analysis, and nuclear magnetic resonance study. *Engineering Reports*. 2021;e12375. https://doi.org/10.1002/eng2.12375